Canted magnetic ground state of quarter-doped manganites $R_{0.75}Ca_{0.25}MnO_3$ (R=Y, Tb, Dy, Ho, and Er)

2017 J. Phys.: Condens. Matter 29 065802

(http://iopscience.iop.org/0953-8984/29/6/065802)

IOP Publishing Journal of Physics: Condensed Matter

J. Phys.: Condens. Matter **29** (2017) 065802 (11pp) doi:10.1088/1361-648X/aa4de1

Canted magnetic ground state of quarter-doped manganites $R_{0.75}Ca_{0.25}MnO_3$ (R = Y, Tb, Dy, Ho, and Er)

R Sinclair[1], H B Cao[2], V O Garlea[2], M Lee[3,4], E S Choi[4], Z L Dun[1], S Dong[5], E Dagotto[1,6] and H D Zhou[1,4]

[1] Department of Physics and Astronomy, University of Tennessee, Knoxville, TN 37996-1200, USA
[2] Quantum Condensed Matter Division, Oak Ridge National Laboratory, Oak Ridge, TN 37831, USA
[3] Department of Physics, Florida State University, Tallahassee, FL 32306, USA
[4] National High Magnetic Field Laboratory, Florida State University, Tallahassee, FL 32310, USA
[5] Department of Physics, Southeast University, Nanjing 211189, People's Republic of China
[6] Materials Science and Technology Division, Oak Ridge National Laboratory, Oak Ridge, TN 37831, USA

E-mail: sdong@seu.edu.cn and hzhou10@utk.edu

Received 6 July 2016, revised 8 November 2016
Accepted for publication 15 November 2016
Published 21 December 2016

Abstract

Polycrystalline samples of the quarter-doped manganites $R_{0.75}Ca_{0.25}MnO_3$ (R = Y, Tb, Dy, Ho, and Er) were studied by x-ray diffraction and AC/DC susceptibility measurements. All five samples are orthorhombic and exhibit similar magnetic properties: enhanced ferromagnetism below T_1 (~80 K) and a spin glass (SG) state below T_{SG} (~30 K). With increasing R^{3+} ionic size, both T_1 and T_{SG} generally increase. The single crystal neutron diffraction results on $Tb_{0.75}Ca_{0.25}MnO_3$ revealed that the SG state is mainly composed of a short-range ordered version of a novel canted (i.e. noncollinear) antiferromagnetic spin state. Furthermore, calculations based on the double exchange model for quarter-doped manganites reveal that this new magnetic phase provides a transition state between the ferromagnetic state and the theoretically predicted spin-orthogonal stripe phase.

Keywords: magnetic materials, magnetoelectrics, spin glass

(Some figures may appear in colour only in the online journal)

1. Introduction

Recent research in the field of manganites has primarily focused on the multiferroic properties of $RMnO_3$ [1–9]. This includes studies of Type-I multiferroics employing materials such as the hexagonal $YMnO_3$ where ferroelectricity and magnetism have different origins [10], and also studies of Type-II multiferroics as in the cases of $TbMnO_3$ and orthorhombic $HoMnO_3$ where the ferroelectricity is caused by peculiar magnetic orders [11–13]. All of these multiferroic $RMnO_3$ materials are located in the narrow-bandwidth limit of manganites due to their small R^{3+} ionic size [14]. The fact that in Type-II multiferroics the ferroelectricity is strongly coupled to magnetism makes it very exciting to explore the possibility of new magnetic states in narrow-bandwidth systems. Discovering exotic magnetic phases may lead to functional multiferroics with high transition temperatures and large spontaneous polarizations.

While the cases of pure undoped manganites have been extensively studied [15, 16], the recent exploration for potential new magnetic phases has focused on doped manganites in the narrow-bandwidth limit [17, 18]. The competition between the ferromagnetic double exchange interactions and the antiferromagnetic superexchange interactions, plus the robust Jahn–Teller spin-lattice coupling, makes the doped narrow-bandwidth manganites an ideal playground to search for new magnetic phases [19]. Moreover, considerable theoretical progress has been made in this area of research. For

example, the magnetic phase diagram of quarter-doped manganites has been investigated based on the double exchange model [20]. A prominent ferromagnetic (FM) metallic orbitally-disordered phase occupies the region where the super-exchange interaction between the t_{2g} spins, J_{AFM}, is small in agreement with the phase diagram of large and intermediate bandwidth manganites. However, a new exotic multiferroic phase, dubbed the spin-orthogonal-stripe (SOS) phase, was found at the large J_{AFM} end of the narrow-bandwidth manganites. The SOS state, as shown in figure 2(a) of [20], is made of zigzag chains, as in the CE-phase of manganites at quarter doping, but forming an array of diagonally oriented domains with spins rotated by 90° between domains. Generalizations to other hole dopings have been studied as well [21].

The intriguing prediction of an SOS state requires detailed experimental studies. Although a couple of previous efforts have been reported for the doped manganites with small R^{3+} ions, such as $Tb_{1-x}Ca_xMnO_3$ [22–27], $Dy_{1-x}Ca_xMnO_3$ [28], and $Y_{1-x}Ca_xMnO_3$ [29, 30], a systematic exploration of quarter-doped manganites $R_{0.75}Ca_{0.25}MnO_3$ has not been conducted and, for this reason, the existence of the SOS phase, or other exotic magnetic phases, has not been confirmed so far. Moreover, theoretically the nature of the quarter-doped manganites with an intermediate J_{AFM} strength has not been studied in full detail. It is only known that the FM and SOS states are stable in the limits of small and large J_{AFM}, respectively [20]. Thus, an intriguing question develops: does any new magnetic phase exist in the intermediate coupling region in between the FM and the predicted SOS phases? Plenty of previous theoretical studies have consistently shown that manganites in general, i.e. not only multiferroics, have the potential to display a wide variety of complex patterns of spin, charge, and orbital order [31–35].

With this timely fresh motivation in mind to search for possible new magnetic phases of quarter-doped manganites with a narrow-bandwidth, in this publication we have systematically studied the magnetic characteristics of $R_{0.75}Ca_{0.25}MnO_3$ (R = Tb, Dy, Ho, Y, and Er). First, we analyzed the magnetic properties of all five polycrystalline samples and found that their general behavior consists of enhanced FM interactions below 80 K and a spin glass state below 30 K. Second, we performed neutron scattering experiments on a single crystal of $Tb_{0.75}Ca_{0.25}MnO_3$ and discovered that its magnetic ground state is dominated by the short-range ordering of a new canted spin state which results in the observed spin glass-like behavior. Finally, we conducted theoretical calculations based on the double exchange model confirming that the observed new spin structure is lower in energy than both the FM and SOS states in the intermediate strength region of J_{AFM}; in other words, the novel magnetic phase reported here acts as a transition state between the FM and the SOS phases.

2. Experimental details

Polycrystalline samples of $R_{0.75}Ca_{0.25}MnO_3$ (R = Tb, Dy, Ho, Y, and Er) were synthesized by solid state reactions. The stoichiometric mixture of $Tb_4O_7/Dy_2O_3/Ho_2O_3/Y_2O_3/Er_2O_3$, $CaCO_3$, and Mn_2O_3 were ground together and then calcined in air at 950 °C, 1200 °C, and 1350 °C for 24 h, respectively. Single crystals of $Tb_{0.75}Ca_{0.25}MnO_3$ were grown by the traveling-solvent floating-zone (TSFZ) technique in an IR-heated image furnace (NEC) equipped with two halogen lamps and double ellipsoidal mirrors. The crystal growth rate was 15 mm h^{-1}. Small pieces of single crystals were ground into a fine powder for x-ray diffraction. The resulting powder x-ray diffraction (XRD) patterns were recorded at room temperature with a HUBER Imaging Plate Guinier Camera 670 with Ge monochromatized Cu $K_{\alpha 1}$ radiation (1.540 59 Å). The lattice parameters were refined from the XRD patterns by using the software package *FullProf Suite* [36] with typical refinements for all samples having $\chi^2 \approx 1 \sim 2$. X-ray Laue diffraction was used to align the crystals. Elastic neutron scattering measurements were performed at the neutron powder diffractometer (HB-2A), and single-crystal neutron scattering measurements were performed at the four-circle diffractometer (HB-3A). The single crystal diffraction data were collected with the wavelength of 1.003 Angstrom from a bent perfect Si-331 monochromator [37]. Both instruments are located at the High Flux Isotope Reactor (HFIR) in Oak Ridge National Laboratory (ORNL). The neutron scattering diffraction patterns were also refined using *FullProf Suite*. The DC magnetic-susceptibility measurements were performed employing a Quantum Design superconducting interference device (SQUID) magnetometer. The AC susceptibility data was measured on a homemade setup [38].

3. Results

3.1. Polycrystalline $R_{0.75}Ca_{0.25}MnO_3$

Figures 1(a)–(e) display the room temperature XRD patterns for $R_{0.75}Ca_{0.25}MnO_3$ (R = Tb, Dy, Ho, Y, and Er). All samples show a pure orthorhombic (*Pbnm*) structure. With decreasing ionic size R, the lattice parameters decrease, as shown in figure 1(f). Furthermore, the room temperature atomic positions, lattice parameters, and occupancies derived from the refinements are shown in table 1 along with the calculated χ^2 value and the overall B-factor used in each refinement. The attempts to prepare orthorhombic $R_{0.75}Ca_{0.25}MnO_3$ with R^{3+} ions smaller than Er^{3+} failed. Noting that pure $HoMnO_3$, $YMnO_3$, and $ErMnO_3$ have hexagonal structures, it seems that the substitution of Ca^{2+} can stabilize the perovskite structure. This is easy to understand since Ca^{2+} ions are larger than the R^{3+} ions involved here and this doping will reduce the manganese size. Therefore, the structural tolerance factor (t) will be increased and, generally, as t increases the driving force for the octahedral rotation increases as well, leading to the transformation from the hexagonal to the orthorhombic phase. Several reported studies on $Ho_{1-x}Ca_xMnO_3$ and $Y_{1-x}Ca_xMnO_3$ have confirmed this observation [17, 30, 39].

Figure 2 shows the temperature dependent DC susceptibility (χ) results corresponding to $R_{0.75}Ca_{0.25}MnO_3$. For the case of $Tb_{0.75}Ca_{0.25}MnO_3$, χ shows two major features: (i) a sharp increase around 80 K with decreasing temperature. This feature

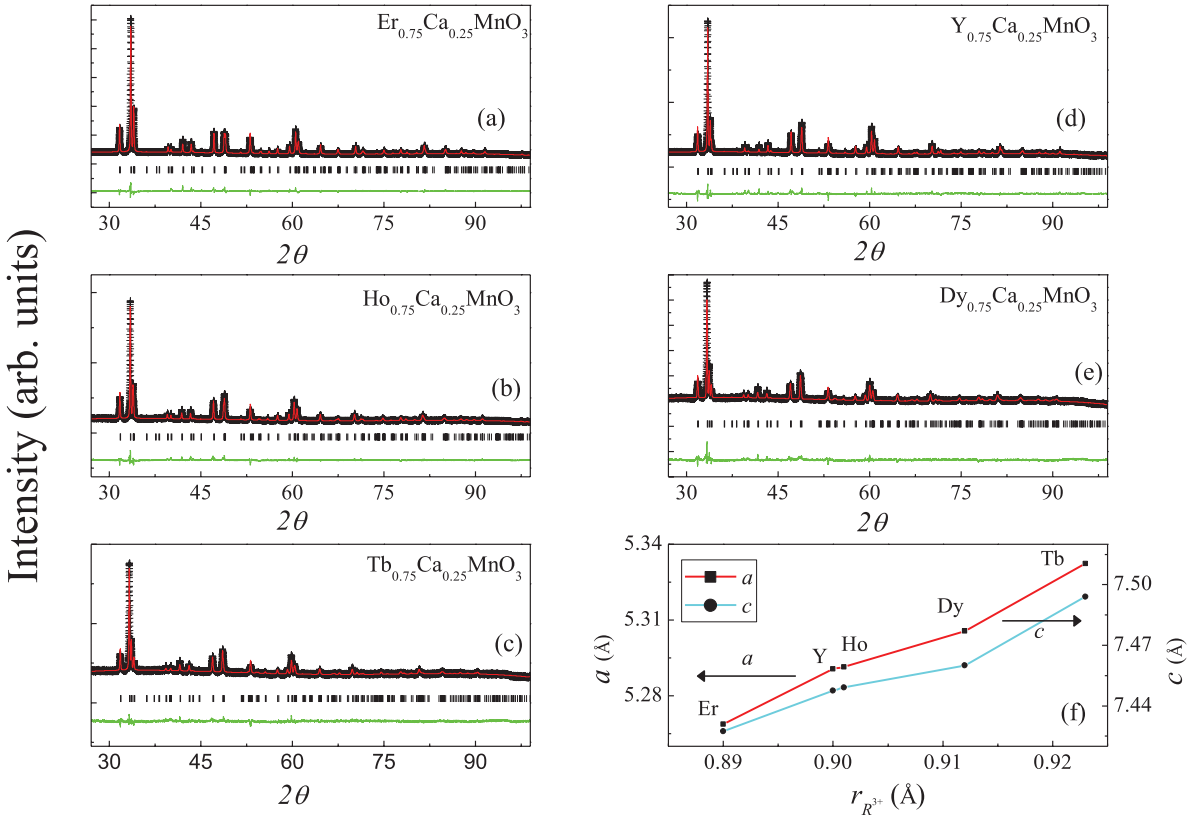

Figure 1. Room temperature XRD patterns for polycrystalline $R_{0.75}Ca_{0.25}MnO_3$: (a) Er, (b) Ho, (c) Tb, (d) Y, and (e) Dy. The crosses are the experimental data. The solid curves are the best fits from the Rietveld refinement using *FullProf Suite*. The vertical marks indicate the position of the Bragg peaks, and the bottom curves show the difference between the observed and calculated intensities. (f) The R^{3+} ionic size dependence of the lattice parameters.

is more evident as a slope change from the linear temperature dependence of the inverse of the susceptibility (figure 2(f)). Here we define the peak position of the derivative of $1/\chi$ as T_1. Clearly, ferromagnetic tendencies develop below T_1; (ii) a broad peak around 34 K where zero field cooling (ZFC) and field cooling (FC) curves display a large splitting. This peak position is defined as T_{SG}. As shown in figure 3, with increasing R^{3+} ionic size, both T_1 and T_{SG} generally increase. One important point here is that since $Y_{0.75}Ca_{0.25}MnO_3$ with nonmagnetic Y^{3+} ions display these two features, they must be related to the magnetic Mn^{3+}/Mn^{4+} ions. To further investigate the magnetic properties, we performed a Curie–Weiss fit on the $1/\chi$ data, as shown in figure 2(i), resulting in a Curie temperature of $\theta_{CW} = 58.1$ K and an effective magnetic moment of $\mu_{eff} = 5.16\,\mu_B$. For $Y_{0.75}Ca_{0.25}MnO_3$, there are 75% Mn^{3+} ions ($\mu_{eff} \approx 4.8\,\mu_B$) and 25% Mn^{4+} ions ($\mu_{eff} \approx 3.8\,\mu_B$) in the system, resulting in an expected total effective moment of $\mu_{eff} \approx 4.6\,\mu_B$ which is consistent with our crude fitting analysis.

Moreover, figure 4 shows the field-dependent DC magnetization data. Clear hysteresis loops can be seen for all five polycrystalline samples at $T = 5.0$ K which indicates the presence of ferro or ferri-magnetic domains in these samples at low temperatures. Although the loops have differing sizes due to the varying rare earth elements in the materials, the existence of the hysteresis loop in the $R = Y$ sample strongly suggests that these ferro or ferri-magnetic domains originate from the Mn ions as the Y^{3+} ions are nonmagnetic.

The AC susceptibility was measured for $Tb_{0.75}Ca_{0.25}MnO_3$ to study the nature of the transition at T_{SG}. As shown in figure 5(a), around T_{SG} the AC susceptibility presents a frequency dependent peak. The Mydosh parameter $\Delta T_{SG}/[T_{SG}\Delta\log(f)]$, a quantitative measure of the frequency shift, is estimated to be 0.034 (figure 5(b)). This is of the same order as the expected range of 0.004–0.018 for conventional spin glass systems [40]. This result is consistent with the DC susceptibility ZFC and FC splitting feature shown in figure 2 which is also a characteristic behavior of a spin glass transition. Moreover, the AC susceptibility also reveals a small feature around $T \sim 50$ K which suggests a possible intermediate short-range ordering for the $R = Tb$ system. This is further supported from the ZFC DC susceptibility data presented in figure 2(a) which shows a broad feature centered near $T \sim 50$ K. From our presented data, this phenomenon appears to be unique to the $R = Tb$ sample.

The powder neutron diffraction measurements were performed on $Tb_{0.75}Ca_{0.25}MnO_3$, and the differential scattering results are shown in figure 6. The large feature near $Q = 2.8$ Å^{-1} is due to the change in lattice parameters. The negative differential signal at $Q < 0.5$ Å^{-1} is caused by the reduction in the paramagnetic scattering that exists above the ordering temperature. Note that the paramagnetic scattering follows the

Table 1. Structural parameters for the $R_{0.75}Ca_{0.25}MnO_3$ samples (R = Y, Tb, Dy, Ho, and Er) at room temperature (space group *Pbnm*) determined from refined XRD measurements.

Refinement	Atom	Site	x	y	z	Occupancy
XRD	Y	4c	−0.016 90(44)	0.072 30(22)	1/4	0.373 65(97)
R = Y	Ca	4c	−0.016 90(44)	0.072 30(22)	1/4	0.126 35(97)
$\chi^2 = 2.10$	Mn	4b	1/2	0	0	0.50
(a)	O1	4c	0.129 22(86)	0.442 01(96)	1/4	0.50
	O2	8d	0.725 06(76)	0.276 44(73)	0.028 81(71)	1.00
	a = 5.290 58(7) (Å), b = 5.626 03(8) (Å), c = 7.447 59(9) (Å)					
	Overall B-factor = 1.4527 (Å^2)					
XRD	Tb	4c	−0.010 915(75)	0.073 91(40)	1/4	0.374 03(97)
R = Tb	Ca	4c	−0.019 15(75)	0.073 91(40)	1/4	0.125 97(95)
$\chi^2 = 1.12$	Mn	4b	1/2	0	0	0.50
(b)	O1	4c	0.084 83(98)	0.456 82(92)	1/4	0.50
	O2	8d	0.724 01(89)	0.281 39(99)	0.020 36(93)	1.00
	a = 5.332 29(14) (Å), b = 5.627 92(16) (Å), c = 7.493 93(19) (Å)					
	Overall B-factor = 2.4558 (Å^2)					
XRD	Dy	4c	−0.009 83(57)	0.068 15(36)	1/4	0.346 40(94)
R = Dy	Ca	4c	−0.009 83(57)	0.068 15(36)	1/4	0.153 60(94)
$\chi^2 = 1.74$	Mn	4b	1/2	0	0	0.50
(c)	O1	4c	0.129 26(83)	0.418 67(94)	1/4	0.50
	O2	8d	0.777 38(86)	0.278 79(95)	0.012 97(89)	1.00
	a = 5.305 60(14) (Å), b = 5.610 14(16) (Å), c = 7.460 11(19) (Å)					
	Overall B-factor = 2.4367 (Å^2)					
XRD	Ho	4c	−0.017 68(37)	0.068 68(19)	1/4	0.372 44(69)
R = Ho	Ca	4c	−0.017 68(37)	0.068 68(19)	1/4	0.127 56(69)
$\chi^2 = 1.55$	Mn	4b	1/4	0	0	0.50
(d)	O1	4c	0.115 28(96)	0.477 19(92)	1/4	0.50
	O2	8d	0.738 01(99)	0.286 01(87)	0.026 53(90)	1.00
	a = 5.291 45(7) (Å), b = 5.640 01(7) (Å), c = 7.449 08(9) (Å)					
	Overall B-factor = 1.4568 (Å^2)					
XRD	Er	4c	−0.018 95(26)	0.072 18(15)	1/4	0.374 92(51)
R = Er	Ca	4c	−0.018 95(26)	0.072 18(15)	1/4	0.125 08(51)
$\chi^2 = 1.68$	Mn	4b	1/4	0	0	0.50
(e)	O1	4c	0.110 89(96)	0.458 40(98)	1/4	0.50
	O2	8d	0.737 36(92)	0.297 03(74)	0.032 06(64)	1.00
	a = 5.268 79(6) (Å), b = 5.646 77(6) (Å), c = 7.427 34(7) (Å)					
	Overall B-factor = 0.7002 (Å^2)					

Q dependence of the Mn^{3+}/Mn^{4+} magnetic form factor. The observed magnetic peak at $Q = 1.6$ Å^{-1} at 40 K (figure 6(a)) is broader than the instrument resolution. Its position suggests it is due to scattering from a short-range ferromagnetic ordering that contributes to the (1 1 0) or (0 0 2) Bragg peaks which can be explained by a ferromagnetic ordering along either the a or b axes. This is consistent with the DC susceptibility results showing the development of ferromagnetism below T_1. Figure 6(b) contains the differential scattering between 4 K and 120 K. The data shows more pronounced scattering that adds to the (1 1 0) or (0 0 2) peaks. In addition, there is another new magnetic peak at $Q = 1.2$ Å^{-1}, matching the (1 0 0) peak position. The presence of this lattice forbidden (1 0 0) peak should be associated with the development of an antiferromagnetic ordering. It is noteworthy that even at 4 K, these peaks are still broader than the instrument resolution, and the correlation length derived from the (1 0 0) Lorentzian full peak width at half maximum is approximately $\xi = 50$ Å.

Therefore, it is concluded that $Tb_{0.75}Ca_{0.25}MnO_3$ develops ferromagnetic characteristics below T_1 and enters a short-range ordered state below T_{SG}, but the latter contains antiferromagnetic tendencies. Based on the similarity among the DC susceptibility measurements of all the $R_{0.75}Ca_{0.25}MnO_3$ samples, this development of magnetism in the Tb sample should occur in all the other samples as well.

3.2. Single crystal $Tb_{0.75}Ca_{0.25}MnO_3$

In order to further clarify the nature of the magnetic properties of $R_{0.75}Ca_{0.25}MnO_3$, we tried to grow single crystals for more

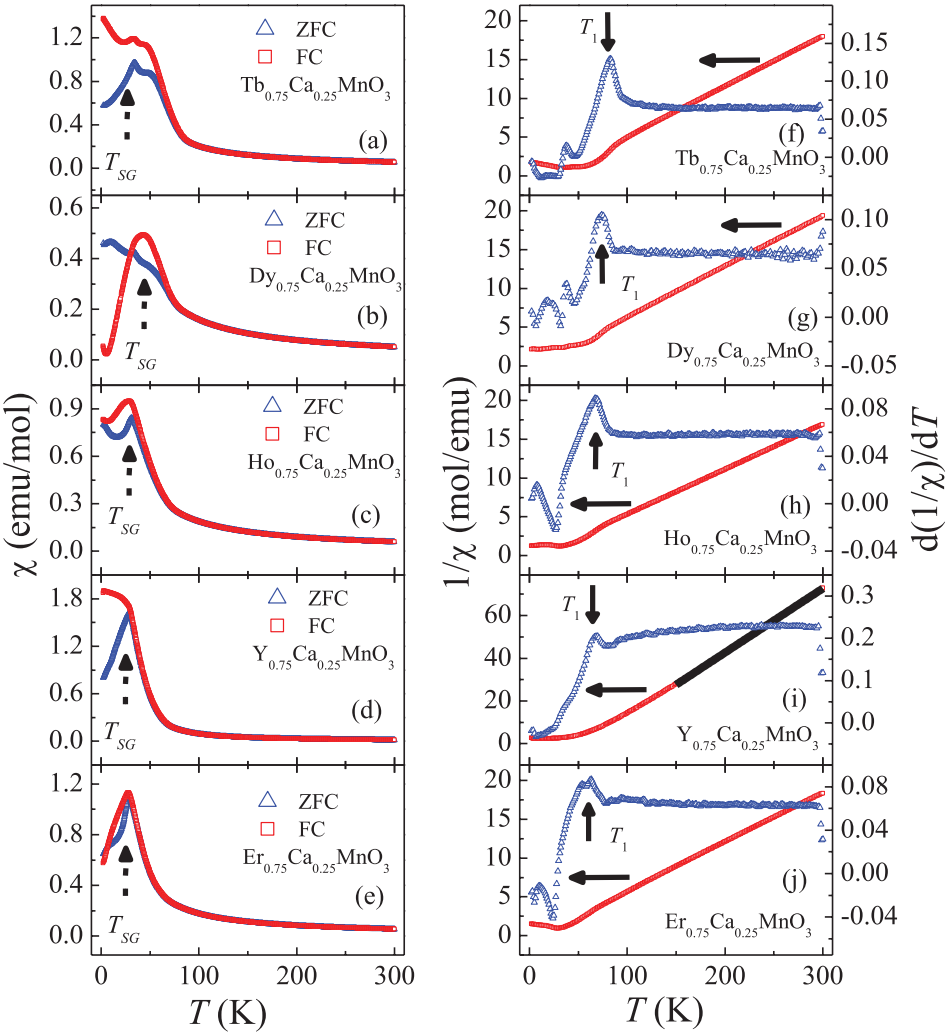

Figure 2. Temperature dependence of the DC susceptibility for polycrystalline $R_{0.75}Ca_{0.25}MnO_3$ measured at $H = 0.01$ T: (a) Tb, (b) Dy, (c) Ho, (d) Y, and (e) Er. Temperature dependence of the inverse of the susceptibility and its derivative for (f) Tb, (g) Dy, (h) Ho, (i) Y, and (j) Er. In (i), the linear solid line represents the Curie–Weiss fit for the $T > 150$ K data.

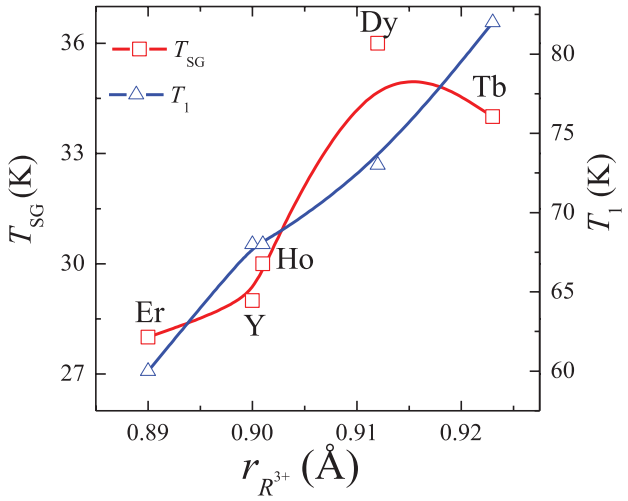

Figure 3. Variations of the T_1 and T_{SG} temperatures with the R^{3+} ionic size for the $R_{0.75}Ca_{0.25}MnO_3$ materials studied here.

detailed studies. We successfully grew single crystals of $Tb_{0.75}Ca_{0.25}MnO_3$ by using the floating zone technique. The obtained crystals cleave easily into several millimeter-long needle pieces. The attempts to grow other $R_{0.75}Ca_{0.25}MnO_3$ samples all failed. Notably, after melting at high temperatures, the Ho, Y, and Er samples show phase separation by introducing the hexagonal phase into the orthorhombic phase. This fact suggests that the orthorhombic phase of the Ho, Y, and Er samples is a meta-stable phase at low temperatures.

Figure 7 shows the DC susceptibility of the $Tb_{0.75}Ca_{0.25}MnO_3$ single crystal with an applied magnetic field H along different axes. For $H\|a$ and $H\|c$, the results for χ are similar between the two data sets which show a slope change around 80 K, as defined by the peak obtained from the derivative of $1/\chi$, and a ZFC and FC splitting around 30 K. These features are consistent with the polycrystalline results. For $H\|b$, the χ results are different from those corresponding to $H\|a$ and $H\|c$. The sharp increase of χ now shifts to around 50 K, and the FC curve keeps increasing below 30 K.

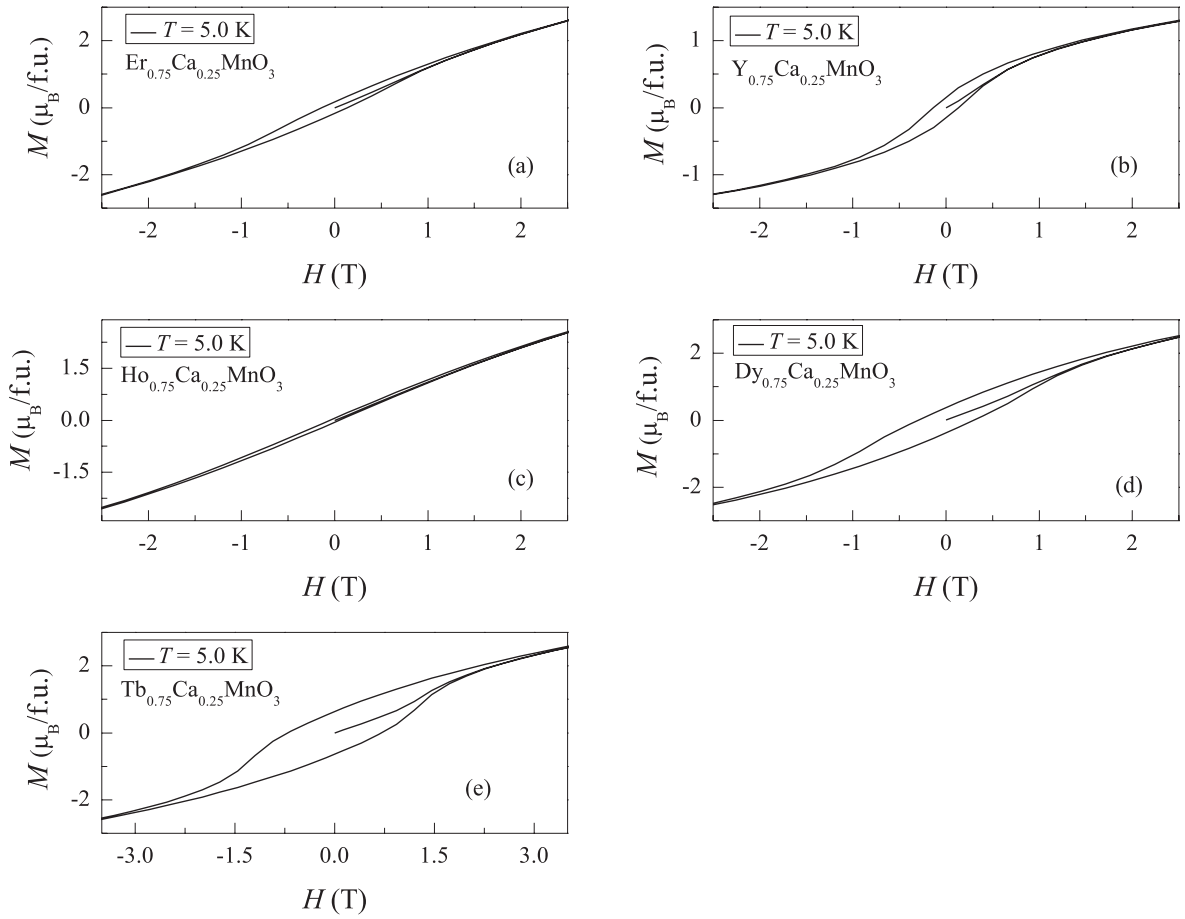

Figure 4. Field dependence of the DC magnetization for polycrystalline $R_{0.75}Ca_{0.25}MnO_3$: (a) Er, (b) Y, (c) Ho, (d) Dy, and (e) Tb samples, all measured at $T = 5.0$ K.

While not shown here, the temperature dependent resistance measured with $H = 0.0$ T and 7.0 T for the single crystal $Tb_{0.75}Ca_{0.25}MnO_3$ sample shows no magnetoresistance. On the other hand, the temperature study of the dielectric constant measured at $H = 0.0$ T and 7.0 T revealed a weak dependence on the magnetic field below $T = 25$ K which can be seen in figure 8. Moreover, the pyroelectric current measurements show no signal for spontaneous polarization related to ferroelectricity (not shown here). As a result, single crystal $Tb_{0.75}Ca_{0.25}MnO_3$ exhibits weak magnetoelectric properties but no ferroelectricity.

Figure 9 displays two magnetic peaks measured by the single crystal neutron diffraction on $Tb_{0.75}Ca_{0.25}MnO_3$ with temperatures: (i) a weak broad peak around the antiferromagnetic Bragg position (1 0 2); (ii) a strong broad peak around the ferromagnetic Bragg position (0 0 2). The temperature dependence of the intensity of the (1 0 2) peak shows that it develops below 35 K, which is around T_{SG}. Meanwhile, the intensity of the shoulder of the (0 0 2) peak at $\theta = 6.5°$ starts developing below 80 K (T_1) and sharply increases below 35 K. These features are consistent with the powder neutron diffraction results. The complete data set was collected at 4.2 K. The nuclear structure refinement using 236 reflections confirms that the crystal structure fits the *Pbnm* symmetry with quarter doping. Seven magnetic reflections (table 2) were obtained by subtracting the nuclear scattering that was measured at 100 K, above the magnetic transition, from the data measured at 4.2 K. Representational analysis using *BasIrreps* in the *FullProfSuite* software package yields 4 allowed magnetic symmetries: *Pbnm*, *Pb′n′m*, *Pbn′m′*, and *Pb′nm′*. Since the ferromagnetic signal was observed at (0 0 2), there must exist a ferromagnetic component perpendicular to the *c*-axis in the ordered magnetic structure (neutrons only see the spins perpendicular to the scattering *Q*). Only *Pbn′m′* and *Pb′nm′* allow the ferromagnetic component to be perpendicular to the *c*-axis, and so we can exclude the other two symmetries. The strong antiferromagnetic signal at (1 0 0) and weak signal at (0 1 0) indicate that the AFM component is mainly along the *b*-axis. Therefore, the *Pbn′m′* is the only magnetic symmetry which matches the observed neutron data. The data refinement based on 7 magnetic peaks using *Pbn′m′* symmetry yields the goodness of fit variable $\chi^2 = 1.10$. The observed and calculated intensities match closely as shown in table 2. The magnetic moments obtained from the refinement are shown in table 3.

The details of the obtained spin structure are shown in figure 10. Here, we see that the Mn spins are canted both in and out of the *a*-*b* plane with canting angles of ∼77° and ∼32°, respectively. The total refined moment of the system was 3.689 μ_B, as shown in table 3, smaller than our crude Curie–Weiss fit but still robust. This spin structure is different from the canonical A-type, E-type, CE-type, C-type, G-type, and spiral-type antiferromagnetic phases observed in manganites

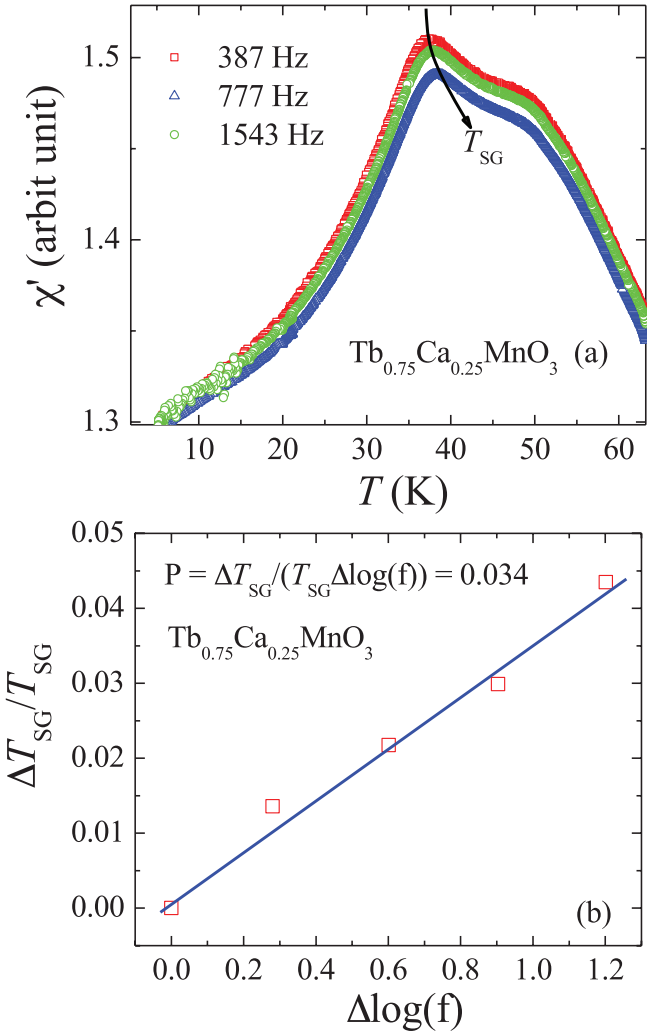

Figure 5. (a) Temperature dependence of the real part of the AC susceptibility for polycrystalline $Tb_{0.75}Ca_{0.25}MnO_3$ under different frequencies. (b) The frequency dependence of $\Delta T_{SG}/T_{SG}$.

before (using the canonical notation [41, 42]). Note, this is a short-range ordered magnetic structure as indicated by the broad characteristics of the magnetic peaks. Using the width of the nuclear peak above the magnetic transition as the instrument resolution, we can derive a magnetic correlation length of ∼123 Å.

4. Discussion

Only a few previous studies of narrow bandwidth $R_{1-x}Ca_xMnO_3$ have addressed the magnetic properties of $R_{0.75}Ca_{0.25}MnO_3$ [17, 20]. For example, Blasco *et al* analyzed $Tb_{1-x}Ca_xMnO_3$ and they showed that with increasing Ca doping the ferromagnetic interactions are enhanced while the antiferromagnetic ordering is suppressed, and in particular the $x = 0.25$ sample has a spin glass ground state [22]. Pena *et al* focused on $Dy1–xCaxMnO_3$, and they also showed an enhanced ferromagnetic interaction around 80 K for the $x = 0.25$ sample [28]. In addition, a neutron powder diffraction study of $Y_{0.7}Ca_{0.3}MnO_3$, which has a similar composition as the $Y_{0.75}Ca_{0.25}MnO_3$ case studied here, shows that the magnetic ground state has short-range ordering

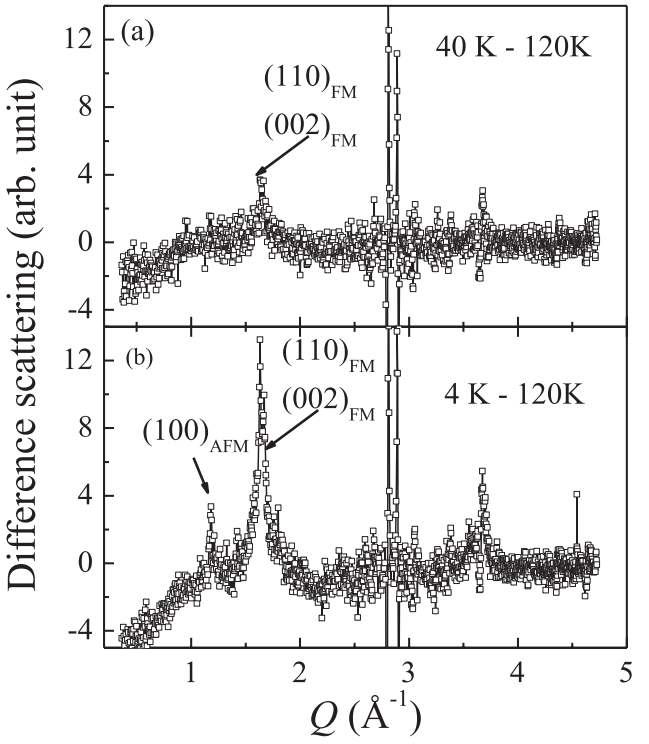

Figure 6. The differential scattering pattern for polycrystalline $Tb_{0.75}Ca_{0.25}MnO_3$ (a) between 40 K and 120 K and (b) between 4 K and 120 K.

with an antiferromagnetic nature due to the observed broad Bragg magnetic peak around the (0 0 1) reflection [30]. Our reported data here is consistent with all of these previous results. More importantly, our systematic studies of $R_{0.75}Ca_{0.25}MnO_3$ point out the presence of enhanced ferromagnetic tendencies around 80 K (T_1) and also the existence of spin glass behavior around 30 K (T_{SG}). Moreover, these are general behaviors for all $R_{0.75}Ca_{0.25}MnO_3$ with $R =$ Tb, Dy, Ho, Y, and Er. With increasing R ionic size, both T_1 and T_{SG} generally increase; in addition, as discussed below the spin glass ground state is compatible with a short-range ordering version of a novel canted ferromagnetic spin state that was unveiled based on our detailed neutron diffraction studies on $Tb_{0.75}Ca_{0.25}MnO_3$ (see figure 10).

To verify the exotic magnetic pattern obtained in our neutron analysis, here a microscopic theoretical study is performed based on the standard two-orbital double-exchange model [41–43]. In the past decade, this model Hamiltonian has been widely used to investigate a plethora of magnetic phases and their associated physical characteristics, such as colossal magnetoresistance and multiferroicity, in perovskite manganites [41, 42]. The clear success of the previous efforts in this context allows us to investigate with confidence the possibility of new phases in previously unexplored regions of the phase diagrams via the double exchange model. More explicitly, the model Hamiltonian used here reads as:

$$H = -\sum_{\langle ij\rangle}^{\alpha\beta} t^{\mathbf{r}}_{\alpha\beta}(\Omega_{ij}\, c^{\dagger}_{i,\alpha}c_{j,\beta} + \text{h.c.}) + J_{\text{AFM}}\sum_{\langle ij\rangle}\mathbf{S}_i\cdot\mathbf{S}_j. \quad (1)$$

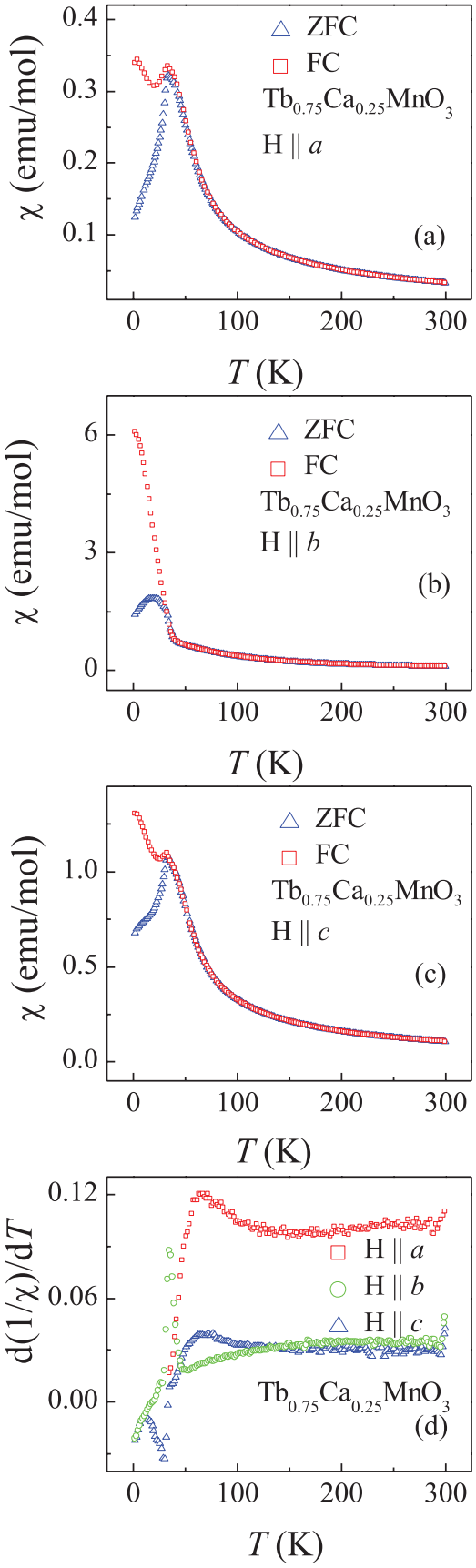

Figure 7. Temperature dependence of the DC susceptibility measured at $H = 0.01$ T for a single crystal of $Tb_{0.75}Ca_{0.25}MnO_3$ with (a) $H\|a$, (b) $H\|b$, and (c) $H\|c$. (d) Derivative of $1/\chi$ with respect to temperature, with H along the three axes.

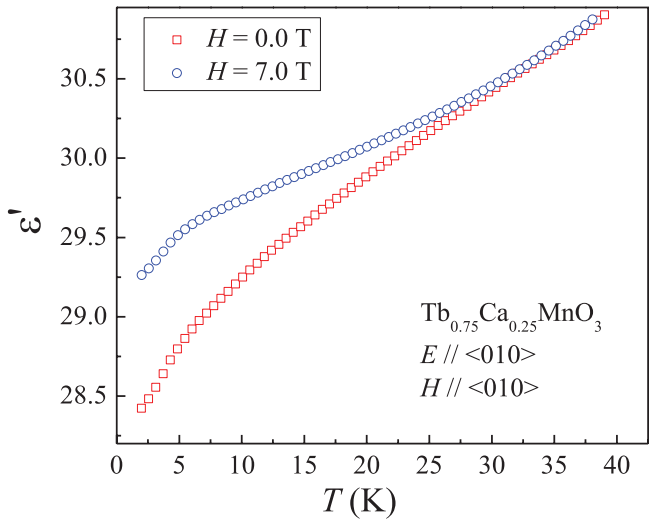

Figure 8. Temperature dependence of the dielectric constant for a single crystal of $Tb_{0.75}Ca_{0.25}MnO_3$ with $H\|b$ and $E\|b$ at $H = 0.0$ T and 7.0 T.

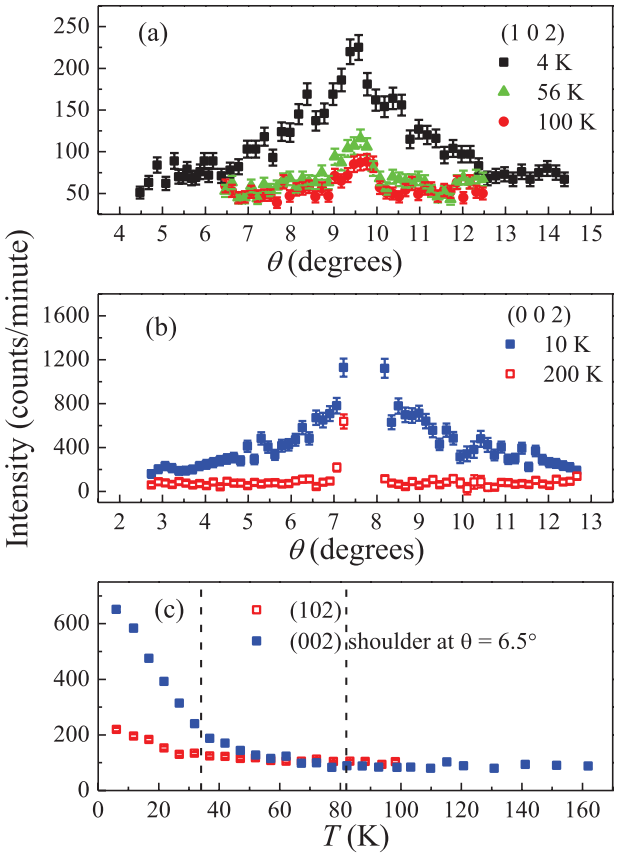

Figure 9. The (a) (1 0 2) and (b) (0 0 2) peaks at different temperatures for the $Tb_{0.75}Ca_{0.25}MnO_3$ single crystal. (c) Temperature dependence of the (1 0 2) peak intensity and the (1 0 2) peak shoulder ($\theta = 6.5°$) intensity.

This Hamiltonian contains two terms. The first term denotes the standard two-orbital double-exchange hopping process for the e_g electrons between nearest-neighbor sites i and j of a three dimensional cubic lattice for the manganese ions. The operators $c^{\dagger}_{i,\alpha}$ ($c_{j,\beta}$) create (annihilate) an e_g electron

Table 2. The observed versus the calculated intensities of the magnetic bragg peaks for single crystal $Tb_{0.75}Ca_{0.25}MnO_3$.

h	k	l	Intensity (observed)	σ	Intensity (calculated)
0	0	2	19.0000	0.82	18.9989
1	0	2	9.5500	0.93	8.4942
1	0	0	10.9100	1.85	11.6812
0	1	2	5.2200	0.78	6.0472
0	1	1	1.7400	0.53	1.7403
2	1	0	7.9700	5.52	5.1609
0	1	0	0.3000	1.00	0.0000

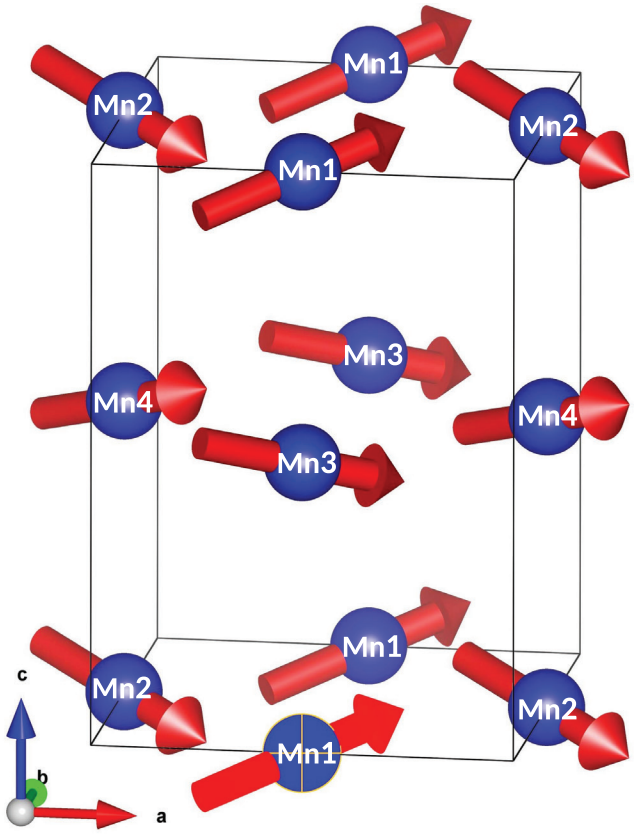

Figure 10. The novel spin state reported for the $Tb_{0.75}Ca_{0.25}MnO_3$ lattice. The manganese sites Mn1, Mn2, Mn3, and Mn4 of table 3 are indicated. There are two canting angles between Mn's nearest-neighbor spins: an in-plane angle of ∼77° and an out-of-plane angle of ∼32°.

at the orbital α (β) of the lattice site i (j). Working within the standard infinite Hund coupling approximation, shown to be qualitatively correct for manganites [41, 42], the spin of the e_g electrons is always parallel to the spin of the localized t_{2g} degrees of freedom, **S**, generating the Berry phase: $\Omega_{ij} = \cos(\theta_i/2)\cos(\theta_j/2) + \sin(\theta_i/2)\sin(\theta_j/2)\exp[-i(\phi_i - \phi_j)]$, where θ and ϕ are the polar and azimuthal angles of the classical t_{2g} spins, respectively [41, 42]. The three nearest-neighbor (NN) hopping directions are denoted by **r**. Two e_g orbitals (a: $x^2 - y^2$ and b: $3z^2 - r^2$) are involved in the double-exchange process for manganites, with the hopping amplitudes along the three axes given by:

$$t^x = \begin{pmatrix} t^x_{aa} & t^x_{ab} \\ t^x_{ba} & t^x_{bb} \end{pmatrix} = \frac{t_0}{4}\begin{pmatrix} 3 & -\sqrt{3} \\ -\sqrt{3} & 1 \end{pmatrix},$$
$$t^y = \begin{pmatrix} t^y_{aa} & t^y_{ab} \\ t^y_{ba} & t^y_{bb} \end{pmatrix} = \frac{t_0}{4}\begin{pmatrix} 3 & \sqrt{3} \\ \sqrt{3} & 1 \end{pmatrix}, \quad (2)$$
$$t^z = \begin{pmatrix} t^z_{aa} & t^z_{ab} \\ t^z_{ba} & t^z_{bb} \end{pmatrix} = t_0\begin{pmatrix} 0 & 0 \\ 0 & 1 \end{pmatrix}.$$

In our calculations, the hopping amplitude t_0 will be considered as the unit of energy. This hopping can be roughly estimated to be 0.5 eV [41, 42]. The second term of the Hamiltonian is the antiferromagnetic superexchange interaction between the NN t_{2g} spins.

The typical value of the superexchange coupling J_{AFM} in manganites is approximately $0.1t_0$ for the more widely studied manganites, such as $La_{1-x}Sr_xMnO_3$ and $La_{1-x}Ca_xMnO_3$, based on a variety of previous investigations [41, 42]. The model studied here does not include the electron-lattice coupling, i.e. the Jahn–Teller distortions, but this coupling can be partially taken into account by increasing the superexchange strength. Our simplified model is expected to capture the main physics of manganites and, thus, can generate a phase diagram qualitatively similar to the experimental observations [44]. Therefore, it is acceptable to study, at least qualitatively, the properties of the manganites discussed in the present publication using this simplified model.

For the quarter-doped manganites, previous investigations predicted a spin-orthogonal stripe SOS phase in the very narrow bandwidth region ($J_{AFM} > 0.17t_0$) [20]. The well known ferromagnetic phase observed in normal manganites appears in the opposite side ($J_{AFM} < 0.13t_0$). In the middle region, the Monte Carlo simulation did not provide an unambiguous answer at that time because of metastabilities in the Monte Carlo time evolution that are typically indicative of complex magnetic patterns [20]. Since the spin pattern obtained in the neutron study discussed above is neither the SOS nor the normal ferromagnetic phases, therefore it is necessary to recheck the possible existence of new phases by taking into account the state discovered experimentally here.

The energies for various fixed magnetic patterns are calculated in momentum space using a fine three dimensional grid and the results are shown in figure 11. With increasing J_{AFM}, the ground state evolves from the initial ferromagnetic state to the final SOS state, in agreement with previous investigations [20]. However, the most interesting new result is that in the middle region ($0.129t_0 < J_{AFM} < 0.161t_0$), the newly discovered canted spin order state displays the lowest energy among all of the candidates investigated here.

According to these results, the case of $Tb_{0.75}Ca_{0.25}MnO_3$ should fall into this middle region. The new canted phase provides a bridge between the ferromagnetic and the SOS phases since it contains both ferromagnetic and noncollinear components. Thus, the pure SOS phase should be expected to be stable only in even narrower bandwidth manganites.

It is worth clarifying that this canted state does *not* induce ferroelectricity if we apply the inverse Dzyaloshinskii–Moriya

Table 3. Magnetic moments for the single crystal $Tb_{0.75}Ca_{0.25}MnO_3$ sample at 4.2 K (magnetic space group *Pbn′m′*) determined from refined neutron diffraction measurements.

	x	y	z	M_x (μ_B)	M_y (μ_B)	M_z (μ_B)	M (μ_B)
Mn1	1/2	0	0	2.89(6)	2.06(8)	1.01(15)	3.689(77)
Mn2	0	1/2	0	2.89(6)	−2.06(8)	−1.01(15)	3.689(77)
Mn3	1/2	0	1/2	2.89(6)	2.06(8)	−1.01(15)	3.689(77)
Mn4	0	1/2	1/2	2.89(6)	−2.06(8)	1.01(15)	3.689(77)

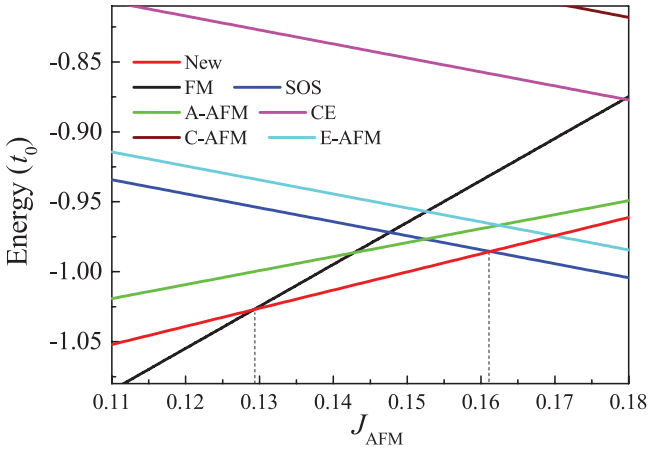

Figure 11. Energies (per site) of the magnetic states considered here, as a function of J_{AFM}. The energy unit is t_0. FM: ferromagnetic; A-AFM: A-type antiferromagnetic; C-AFM: C-type antiferromagnetic; E-AFM: E-type antiferromagnetic. These antiferromagnetic as well as the CE labels are standard notations in manganites [41, 42]. The SOS state is from [20]. The novel canted state is denoted by 'New'.

(DM) mechanism where lattice distortions leading to ferroelectricity are generated by special noncollinear magnetic states [11]. In the present case the local displacements will compensate between nearest neighbors, and the global ferroelectric polarization will cancel out. Although not ferroelectric, the noncoplanar spin texture of the state unveiled here is very novel, and it can give rise to an intrinsic anomalous Hall effect [45, 46].

5. Conclusions

In this publication, we report detailed experimental studies of $R_{0.75}Ca_{0.25}MnO_3$ (R = Y, Tb, Dy, Ho, and Er) polycrystals and a $Tb_{0.75}Ca_{0.25}MnO_3$ single crystal, with focus on their magnetic and electric properties. The amount of Ca used corresponds to the hole quarter-doped case of the widely discussed manganite multiferroic perovskites. In general, we have observed the presence of ferromagnetic and spin-glass tendencies in all of the samples studied. Our main discovery, using the Tb-based single crystal, is that the spin-glass region appears dominated by the short-range order of a new canted, and thus noncollinear, magnetic state. The theoretical study of the double-exchange model presented here shows that in a reduced region of parameter space the new state has indeed lower energy than the two states previously believed to be dominant at quarter doping in narrow bandwidth manganites, namely the FM and SOS states. The results reported here illustrate that doped manganite multiferroic compounds harbor magnetic states that are more complex than previously anticipated. Our present efforts are expected to pave the way and motivate more detailed studies of these mainly unexplored exotic materials that have potential for functional applications.

Acknowledgments

RS, ZLD, and HDZ thank the support from NSF-DMR through Award DMR-1350002. The research at HFIR/ORNL was sponsored by the Scientific User Facilities Division (HBC, OVG, JM), Office of Basic Energy Sciences, US Department of Energy. SD was supported by National Natural Science Foundation of China (Grant Nos. 51322206). ED was supported by the National Science Foundation under Grant No. DMR-1404375. The work at NHMFL is supported by Grant No. NSF-DMR-1157490 and the State of Florida and by the additional funding from NHMFL User Collaboration Support Grant.

References

[1] Kimura T, Goto T, Shintani H, Ishizaka T, Arima T and Tokura Y 2003 *Nature* **426** 55
[2] Goto T, Kimura T, Lawes G, Ramirez A P and Tokura Y 2004 *Phys. Rev. Lett.* **92** 257201.
[3] Kenzelmann M, Harris A B, Jonas S, Broholm C, Schefer J, Kim S B, Zhang C L, Cheong S-W, Vajk O P and Lynn J W 2005 *Phys. Rev. Lett.* **95** 087206
[4] Kimura T, Lawes G, Goto T, Tokura Y and Ramirez A P 2005 *Phys. Rev.* B **71** 224425
[5] Arima T, Tokunaga A, Goto T, Kimura H, Noda Y and Tokura Y 2006 *Phys. Rev. Lett.* **96** 097202
[6] Mostovoy M 2006 *Phys. Rev. Lett.* **96** 067601
[7] Lorenz B, Wang Y Q and Chu C W 2007 *Phys. Rev.* B **76** 104405
[8] Hur N, Park S, Sharma P A, Ahn J S, Guha S and Cheong S-W 2004 *Nature* **429** 392
[9] Chapon L C, Blake G R, Gutmann M J, Park S, Hur N, Radaelli P G and Cheong S-W 2004 *Phys. Rev. Lett.* **93** 177402
[10] van Aken B B, Palstra T T M, Filippetti A and Spaldin N A 2004 *Nat. Mater.* **3** 164
[11] Sergienko I A and Dagotto E 2006 *Phys. Rev.* B **73** 094434
[12] Sergienko I A, Şen C and Dagotto E 2006 *Phys. Rev. Lett.* **97** 227204
[13] Picozzi S, Yamauchi K, Sanyal B, Sergienko I A and Dagotto E 2007 *Phys. Rev. Lett.* **99** 227201
[14] Maignan A, Martin C, Van Tendeloo G, Hervieu M and Raveau B 1999 *Phys. Rev.* B **60** 15214

[15] Ishiwata S, Kaneko Y, Tokunaga Y, Taguchi Y, Arima T and Tokura Y 2010 *Phys. Rev.* B **81** 100411
[16] Dong S and Liu J-M 2012 *Mod. Phys. Lett.* B **26** 1230004
[17] Jiang N, Zhang X and Yu Y 2013 *J. Phys.: Condens. Matter* **25** 475901
[18] Yoshii K, Abe H and Ikeda N 2005 *J. Solid State Chem.* **178** 3615
[19] Demir S, Jeon I-R, Long J R and Harris T D 2015 *Coord. Chem. Rev.* **289–90** 149
[20] Dong S, Yu R, Liu J-M and Dagotto E 2009 *Phys. Rev. Lett.* **103** 107204
[21] Liang S, Daghofer M, Dong S, Şen C and Dagotto E 2011 *Phys. Rev.* B **84** 0024408
[22] Blasco J, Ritter C, García J, de Teresa J M, Pérez-Cacho J and Ibarra M R 2000 *Phys. Rev.* B **62** 5609
[23] Mufti N, Nugroho A A, Blake G R and Palstra T T M 2008 *Phys. Rev.* B **78** 024109
[24] Mufti N, Blake G R, Nugroho A A and Palstra T T M 2009 *J. Phys.: Condens. Matter* **21** 452203
[25] Machida A, Moritomo Y, Mori S, Yamamoto N, Ohoyama K, Nishibori E, Takata M, Sakata M, Otomo T and Nakamura A 2002 *J. Phys. Soc. Japan* **71** 27
[26] Machida A, Moritomo Y, Ohoyama K and Nakamura A 2001 *J. Phys. Soc. Japan* **70** 3739
[27] Nugroho A A, Risdiana, Mufti N, Palstra T T M, Watanabe I and Tjia M O 2009 *Physica* B **404** 785
[28] Peña O, Bahout M, Gutierrez D, Duran P and Moure C 2003 *Solid State Sci.* **5** 1217
[29] Sahu J R, Serrao C R, Ghosh A, Sundaresan A and Rao C N R 2009 *Solid State Commun.* **149** 49
[30] Dlouhá M, Vratislav S, Jirák Z, Knížek K and Sedmidubský D 2002 *Appl. Phys. A: Mater. Sci. Process.* **74** S673
[31] Hotta T, Yunoki S, Mayr M and Dagotto E 1999 *Phys. Rev.* B **60** 15009
[32] Hotta T, Moraghebi M, Feiguin A, Moreo A, Yunoki S and Dagotto E 2003 *Phys. Rev. Lett.* **90** 247203
[33] Hotta T, Feiguin A and Dagotto E 2001 *Phys. Rev. Lett.* **86** 4922
[34] Hotta T, Takada Y, Koizumi H and Dagotto E 2000 *Phys. Rev. Lett.* **84** 2477
[35] Dong S, Yu R, Yunoki S, Liu J-M and Dagotto E 2008 *Phys. Rev.* B **78** 155121
[36] Rodriguez-Carvajal J 1993 *Physica* B **192** 55
[37] Chakoumakos B C, Cao H, Ye F, Stoica A D, Popovici M, Sundaram M, Zhou W, Hicks J S, Lynn G W and Riedel R A 2011 *J. Appl. Cryst.* **44** 655
[38] Dun Z *et al* 2015 *Phys. Rev.* B **92** 024408
[39] Rout P P and Roul B K 2013 *J. Mater. Sci.: Mater Electron* **24** 2493
[40] Mydosh J A 1993 *Spin Glasses: an Experimental Introduction* (London: Taylor and Francis)
[41] Dagotto E 2002 *Nanoscale Phase Separation and Colossal Magnetoresistance* (Berlin: Springer)
[42] Dagotto E, Hotta T and Moreo A 2001 *Phys. Rep.* **344** 1
[43] Dagotto E, Burgy J and Moreo A 2003 *Solid State Commun.* **126** 9
[44] Dong S, Zhang X T, Yu R, Liu J-M and Dagotto E 2011 *Phys. Rev.* B **84** 155117
[45] Chen X, Dong S and Liu J-M 2010 *Phys. Rev.* B **81** 064420
[46] Nagaosa N, Sinova J, Onoda S, MacDonald A H and Ong N P 2010 *Rev. Mod. Phys.* **82** 1539